RM-566

INVESTIGATION OF KC-135 FLIGHT SAMPLES SOLIDIFIED IN NEAR-ZERO GRAVITY

January 1973

RESEARCH DEPARTMENT

GRUMMAN AEROSPACE CORPORATION
BETHPAGE NEW YORK

Grumman Research Department Memorandum RM-566

INVESTIGATION OF KC-135 FLIGHT SAMPLES SOLIDIFIED IN NEAR-ZERO GRAVITY[†]

by

D. Larson, Jr.

and

G. Busch

Materials and Structural Mechanics

January 1973

[†]This investigation was partially funded by the National Aeronautics and Space Administration under Contract NAS 8-28728

Approved by: Charles E. Mack, Jr.
Charles E. Mack, Jr.
Director of Research

ABSTRACT

An analysis was conducted of three KC-135 flight samples that had been solidified in near-zero gravity.

These samples had been generated during near-zero gravity testing of M553 Experiment Skylab Flight hardware. The samples evaluated were all Star-J Stellite, a cobalt base alloy.

The analytical procedures (optical microscopy, scanning electron microscopy, electron microprobe, X-ray diffraction, differential scanning calorimetry, and microhardness) to be used on the Skylab flight samples were optimized and the analytical results are presented.

TABLE OF CONTENTS

LIST OF ILLUSTRATIONS

INTRODUCTION

As part of its efforts in the Materials Science and Manufacturing in Space (MS/MS) program, NASA is conducting experiments in the Skylab program with the ultimate goal of manufacturing useful products in space. The M553-Sphere Forming Experiment, to be conducted within the M512 facility of Skylab, has been planned, specified and fabricated. To evaluate the equipment, procedures, and specimen evaluation sequence, experiments were performed on a KC-135 aircraft flown in parabolic arcs to achieve a near-zero-g condition

Three of the material samples used in the KC-135 flights were evaluated by the Grumman Research Department, under NASA Contract (NAS 8-28728). This Memorandum describes the investigation.

EXPERIMENTAL RESULTS AND DISCUSSION

Each of the three samples evaluated was a "Star-J Stellite" castable cobalt base alloy. Before discussing the results, the metallurgy and metallography of the alloy are described to form the basis for comparison with the "zero-g" solidified specimens.

The nominal composition is given in Table 1 (Ref. 1); this

Table 1

NOMINAL COMPOSITION OF STAR-J

Element	Composition (wt.%)
C	2.5 ± 0.2
Si	1.0 max
Mn	1.0 max
Fe	3.0 max
Ni	2.5 max
Cr	32.5 ± 1.5
W	17.5 ± 1.5
Others	2.0 max
Co	Balance

composition is reasonably well represented by the pseudo-quaternary composition given in Table 2. However, since quaternary systems are difficult to portray in two dimensional space, we introduce the further simplification of considering the ternary Co-C-M, where M is a metal element (primarily chromium or tungsten).

Table 2

STAR-J PSEUDO-QUATERNARY COMPOSITION

Element	Composition (wt.%)
C	2.5
Co	47.5
Cr	32.5
W	17.5

The phases found in the earth (1-g) melted Star-J, based on information supplied by the Cabot Corporation (Ref. 2), are listed in Table 3. The presence of these phases allows us to construct a

Table 3

PHASES PRESENT IN STAR-J STELLITE

Phase	Crystal Symmetry	Descriptor
M_7C_3	Rhombohedral	Primary Precipitate and Secondary Precipitate
M_6C	Cubic	Secondary Precipitate
α - Co	Hexagonal	Matrix
$M_{23}C_6$	Cubic	Occurs Rarely

partial ternary phase diagram as shown in Fig. 1a and a representative isopleth as shown in Fig. 1b (Ref. 3). Further, the primary metallic element in the M_7C_3 carbide is expected to be chromium, whereas the principal metallic elements in the ternary M_6C carbide are likely to be cobalt and tungsten. The latter

carbide typically has a range of stoichiometry varying as much as from Co_2W_4C to Co_4W_2C (Ref. 4).

The suggested isopleth should vary somewhat, depending on whether the region solidifying is within the compositional range of Region I or Region II of the ternary triangle (Fig. 1a). If the solidification is within Region I instead of Region II, the M_6C and α phases will be interchanged in Fig. 1b. The primary solidification phase, however, is invariably the M_7C_3 carbide and, depending on whether the solidification is in Region I or II, the secondary crystallization is M_6C or α, respectively. If, through elemental segregation, the tungsten content is significantly reduced, there will also be the possibility of the reaction $Co_4W_2C \rightarrow (Co, W)_{23}C_6$ (Ref. 4), but this is considered to be abnormal behavior (Ref. 2). There is elemental substitution in all of the phases present in this commercial alloy, but the elemental substitution is likely to be most appreciable within the cobalt terminal solid solution. Consequently, at very high temperatures, M will conveniently be considered chromium and, at lower temperatures, tungsten, with the remaining elements found in the α terminal solid solution.

Analysis of as-received Star-J material, for comparison to flight samples, gave the following results:

Microstructure. The microstructure consists of primary M_7C_3 carbides in a ternary eutectic matrix of M_6C, α - Co, and secondary M_7C_3 (Fig. 2). The primary M_7C_3 carbides reflect their rhombohedral crystal symmetry in that their morphology is hexagonal in cross section and needle-like in the longitudinal direction. In the as-received material, nickel was discovered in these carbides in addition to the anticipated chromium. The primary M_7C_3 carbides were almost invariably surrounded by α, which would

indicate that the solidification sequence shown in Fig. 1b is the most common. The subsequent eutectic or secondary carbide crystallization is not as singularly defined morphologically and the M_7C_3 (secondary) and M_6C carbides are difficult to differentiate under the light microscope. The M_6C morphology is sometimes in the form of "chinese script," which results from the growth of secondary phases, in a eutectic reaction, in the form of dendritic skeletons (Ref. 3). Some of these skeletons appear in Fig. 2a, but the balance of the precipitation is not readily identifiable optically as relating to a particular carbide; these particles are of irregular faceted morphologies.

Differentiation of these particles is desirable and the most convenient means for doing so is scanning electron microscopy (SEM) and specimen current imaging with the electron microprobe. Each has a distinct advantage: the former has great latitude in magnification, depth of field, specimen orientation, and resolution, whereas the latter can give an accurate representation of the elemental distribution (microchemistry). The latter may also be done on the SEM if energy dispersive equipment is available. Micrographs representative of Star-J material are shown in Figs. 2b and 2c for SEM and microprobe, respectively. The polarity inversion is by coincidence in this case, and is not meaningful.

Hardness. Star-J is an air-castable alloy of high as-cast hardness. The expected Brinell hardness (Ref. 1) is 620-650 Kg/mm^2. These values were checked utilizing a Reichert microhardness tester and converting to the Brinell scale. The results are shown in Table 4 for each of the principal constituent phases. The hardest phase is the M_7C_3 phase (1340 Brinell); next is the M_6C phase (800 Brinell). Softest is the cobalt terminal solid solution (450 Brinell). The aggregate hardness was found to be in reasonable agreement with the literature.

Table 4

HARDNESS OF STAR-J CONSTITUENT PHASES

Phase	Microbrinell Hardness (kg/mm^2)	Descriptor
M_7C_3	1340	As-Received
M_6C	800	As-Received
α - Co	450	As-Received
M_7C_3	1450	Sample #I, no nickel in primary carbide

Curie Point. The as-received Star-J material is nonmagnetic at room temperature and cycling to as low as -196°C did not cause a ferromagnetic transformation. As this is the lower temperature limit of our equipment, we can only report that the Curie point is below -196°C. A check with the suppliers of this material (Ref. 2) indicated that it would be highly unusual for this castable alloy at room temperature to exhibit a magnetic phase due to elemental segregation.

The following subsections describe our evaluation of the respective KC-135 flight samples.

Sample 13 - Flight 2

Sample 13 from KC-135 flight 2 is a Star-J Stellite retained sample; i.e., it was solidified on a capture sting also made of Star-J Stellite.

The surface structure of the sample indicated a solidification sequence that initiated in the "sting" region. This was a relatively large sample (1.4990 grams); its surface morphology is depicted in Figs. 3a and 3b. This sample demonstrated four discrete surface morphologies that can be qualitatively described as smooth, intermediate, coarse, and an anomalous magnetic bulge.

The smooth region shown in Fig. 3a was located immediately around the capture sting (Figs. 4a and b). It should be noted in Fig. 4a that the region immediately surrounding the sting evidenced no primary M_7C_3 carbides and this could account for the smooth external surface morphology shown in Fig. 4b. This lack of primary M_7C_3 carbide might be due either to the cooling rate or to a microchemical fluctuation that resulted in a eutectic composition in this region. The fluctuation might well have been caused by the preferential melting of the low melting point constituents of the sting.

The region of intermediate surface roughness was characterized microstructurally by regions similar to those shown in Figs. 5a and b. These regions contained primary M_7C_3 carbides and appeared to have growth directions parallel to the specimen surface. The carbides were finer than the as-received material. This would indicate that there was little thermal or mechanical disturbance during the solidification of the outer shell. A thermal gradient would have resulted in a strong radial growth morphology for the M_7C_3 carbides, which was not observed. One aspect of this microstructure that is somewhat unusual is the fan-like array of M_7C_3 carbides in certain regions of Fig. 5a, and in Fig. 5b. These arrays show a crystallographic orientation relationship. The areas between these arrays are almost totally filled, with little evidence of wicking, shrinkage, or evaporative loss (Fig. 5b).

The nodular appearance of the interarray areas may be due to the dendritic solidification of eutectic carbides of the M_6C type.

The coarse surface of this sample is shown in Fig. 6 and is located in the region of the sample that is the last region to solidify. This morphology is due to "stacks" of primary M_7C_3 carbides with void areas between the primary needles. These regions contain reduced quantities of M_6C, α - Co, and secondary M_7C_3 particles, indicating a deficiency of the liquid that would normally result in the secondary and eutectic solidification. The primary M_7C_3 carbides are quite large, which would indicate more time to nucleate and grow than in other regions, and the void areas could be due to either wicking, evaporative loss, or shrinkage.

The bulge region referred to is anomalous in behavior in that it is magnetic. This is a discrete region with well defined boundaries, as shown in Fig. 7a and at higher magnification in Fig. 7b. It was found to be abnormally high in nickel and to contain aluminum, chromium, and cobalt, as well. This indicates the logical origin to be one of contamination by a fragment of the alumina pedestal that came in contact and reacted with the liquid metal. The small globular particles shown in Fig. 7b fluoresced under the electron beam, indicating an oxide phase. This is most likely unreacted alumina from the fragment or a spinel reaction product of the form $(Ni,Co,Fe)O\cdot(Al,Cr)_2O_3$. The dendritic matrix did not fluoresce, indicating a lower oxygen content. This matrix was primarily nickel-aluminum of a magnetic composition, but no effort was made to define quantitatively the phase relationships involved as the region was an artifact of poor melting practice and not related to the specimen material.

One feature that was apparently due to the alumina contamination, but which is of interest nevertheless, is the very high nickel content in this region and the corresponding nickel deficiency in the primary M_7C_3 carbides. Apparently, the affinity of nickel for aluminum is considerably greater than that for chromium or cobalt, and results in the unusual elemental partitioning noted. This partitioning is reflected by the reduced nickel content increasing the M_7C_3 microbrinell hardness from 1340 to 1450.

In summary, we conclude that the most striking feature of this sample was a discrete magnetic region, but that its origin was not related to the zero-g processing. The microstructure varied in a readily predictable fashion, upon consideration of possible variations within composition limits and cooling rates; however, it occurred on a finer scale than that usually found in as-received material.

Sample 23 - Flight 2

This was a small sample of Star-J Stellite that most likely was a piece of a specimen that exploded on heating, although the material appeared to have been fully molten at one time. The sample (0.0451 g) was only about 1/30 the size of the previous sample.

The surface morphologies were entirely as previously described for Sample 13 except that there was no magnetic region and the sample had a minute flat surface, caused by its hitting the chamber wall while insufficiently solid to withstand the impact entirely. The M_7C_3 particles did not "radiate" from this point of impact, which led us to conclude that the solidification was well under way prior to touching the chamber wall. Two aspects of the surface morphology that are worth noting are shown in Figs. 8 and 9.

Figure 8 illustrates a region of coarse surface morphology with substantial interparticle void area. Two features that should be noted are the hollow ends of the primary M_7C_3 carbides and the nodular particles lying underneath and between the M_7C_3 particles. The nodular particles contain both cobalt and tungsten and are most likely end points of the M_6C dendritic skeleton at the sample surface. The reason for the hollow ends of the primary M_7C_3 particles is less obvious, but probably results from crystal growth in the [0001] "C" direction (using hexagonal indices) but on planes other than the basal plane. The most likely planes would be the $\{01\bar{1}0\}$ prismatic planes. Consideration of a growth process limited to this set of planes, and with some broadening in the $\langle\bar{2}110\rangle$ directions in addition to the [0001] primary growth direction, readily explains the hollowed core (empty at the surface and filled internally) that other mechanisms fail to do. This also explains the prismatic growth steps noted on some hexagonal cross sections (see Fig. 2a) as well as most of the atypical cross sections encountered.

Figure 9 is a SEM micrograph in a region that would have been classified as being of intermediate surface roughness. In this case, the primary M_7C_3 carbides are on an extremely fine scale and are intimately dispersed amongst the nodular M_6C particles. This could result from a shorter growth period for the primary M_7C_3 particles, or from uniform nucleation in an alloy that would have a lower volume percentage of proeutectic M_7C_3.

Sample 1 ("Pore" Sample) - Flight 1

When compared to the other two specimens, this Star-J sample, shown in Fig. 10a, had several distinct features worth noting.

- It was dull in appearance, perhaps indicating contamination.
- It was severely flattened on one side due to hitting the chamber wall prior to solidification.
- It had an internal pore that exited to the outer surface at the mid-portion of the "hemisphere."
- The flattened base of the sample was nonmagnetic whereas the "hemispherical" surface was magnetic.
- The internal microstructure could be roughly broken into five distinct regions, as shown photographically in Fig. 10b and schematically in Fig. 10c.

Taking each microstructural region in numerical sequence, they are presented in Fig. 11 in a clockwise fashion, starting at the bottom, and are arrayed about a low magnification micrograph of the sample that shows the regions of interest.

Region I is at the flattened base and was very chemically resistant. The microstructure is extremely fine and the precipitate morphology is such that no primary M_7C_3 precipitates are evident. This change in morphology could be due to a chemical shift resulting in strictly eutectic solidification in this region; however, microprobe analysis of this region did not support this contention (Fig. 14). It is more likely that the morphological change is due to the extremely rapid cooling rate in this region and perhaps as a result of a significant degree of undercooling ($> 170°C$) as well. It has been shown (Ref. 5) that undercooling a eutectic liquid in excess of $170°C$ and subsequent rapid directional solidification results in an extremely fine equiaxed precipitate morphol-

ogy (Fig. 11a). This precipitate structure is on an extremely fine scale with M_6C mean particle diameters as small as 1μm at the flattened surface and gradually increasing to 5μm approximately 200μm into the sample (Fig. 12). From this point inward, the precipitate morphology is significantly different in that radial proeutectic primary M_7C_3 particles are evident and the mean particle diameters increase significantly for both the M_7C_3 and M_6C carbides. M_6C mean particle diameter and number of particles/unit area, shown schematically in Fig. 12, are tabulated in Table 5, and the microstructure of this region is presented in Fig. 13. If rapid, nondiffusional, solidification were present, it would be anticipated that the microchemistry in this region would be very near constant. This is definitely the case within 100μm of the flat surface, but begins to deviate from a constant mean value beyond that point (Fig. 14). This may be a result of increasing particle size relative to the microprobe electron beam (3-5μm in diameter) and may reflect simply an increased deviation from appropriate sampling statistics. In any case, this unique morphological region extends at least 100μm inward and is likely to extend inward as far as 200μm in some regions. A characteristic dimension of the M_7C_3 particles in Fig. 11a is 4.5μm with a maximum diameter of 10.5μm. Figure 11a may be considered to be a region approximately 60μm from the flattened surface. Critical precipitate dimensions for Regions I-IV are tabulated in Table 5. Microbrinnel hardness of this region is 700.

Region II is depicted microstructurally in Fig. 11b and may be considered to begin about 300μm inward from the flattened surface. This region begins to show the radial growth morphology of the primary M_7C_3 carbides, indicating a significant diffusional contribution and enlarged critical dimensions (Table 6).

Table 5

M_6C PARTICLE ANALYSIS OF REGION I, SAMPLE I, FLIGHT I

M_6C Particles/cm^2 #/cm^2	Distance (μm)	Mean Particle Diameter (μm)
4.43×10^6	10	1.25
4.21	20	
4.66	30	2.50
--	40	
3.54	50	
3.54	60	3.75
3.44	70	
3.33	80	
3.54	90	3.75
3.10	100	
3.76	110	
3.54	120	
3.54	130	
2.88	140	
2.66	150	5.00
2.88	160	
2.88	170	
3.10	180	
2.88	190	
2.43	200	
2.88	210	5.00
2.43	220	
2.21	230	
2.43	240	
--	250	
--	260	
1.55	270	15.0
1.33	280	
.37	290	
.99	300	20.0
1.10	310	

Table 6

CRITICAL PARTICLE DIMENSION IN THE DIFFERING REGIONS OF SAMPLE I

Region	Particle Type	Maximum Dimension (μm)	Descriptor
I	M_7C_3	max 10.5 mean 4.5	Transverse
	M_6C	mean 3.0 max 12.0	Transverse
II	M_7C_3	max 15.7	
	M_6C	mean 4.4 max 14.3	
III	M_7C_3	max 24 max 20 μ Probe	
	M_6C	mean 7.5 max 14	
IV	M_6C	mean 12.5 max 18	
As-Rec.	M_7C_3	max 120	
Rough Sfce. Region 13	M_7C_3	max 60	

The maximum transverse diameter of the M_7C_3 primary carbides in this region was 15.7μm, the mean M_6C diameter was 4.4μm, and the maximum M_6C diameter was 14.3μm, for the limited sampling undertaken.

Figure 11c shows the microstructure in the vicinity of the large internal pore (Region III). It is clear that the primary M_7C_3 carbides are greatly enlarged (maximum diameter 24μm) and are comparable to the diameters measured in this region on the electron microprobe (20μm). This morphology is comparable to the region of Sample 13 that demonstrated a coarse surface morphology; however, the largest primary M_7C_3 carbide noted in that sample was 60μm. This was probably due to the greater mass of Sample 13 and the concomitant increase in solidification time of the last liquid. The maximum diameter of a primary M_7C_3 particle in as-received material was 120μm. The M_6C particles were somewhat larger than those in Region II (mean diameter 2.5μm, and 14μm maximum).

Region IV was singled out only because of the well defined M_6C dendritic skeleton (chinese script); this is shown in Fig. 11d. The maximum diameter of these arrays was approximately 18μm and the mean diameter was 12.5μm.

Region V was due to contamination from the pedestal material and is unlike any of the other regions of Sample 1 or the contaminated region of Sample 13. The contaminated regions of Sample 1 were extensive, were very susceptible to corrosive attack (see excessive attack of one constituent in Fig. 11e), and did not strongly fluoresce under the electron microprobe beam, indicating that the oxygen had either been dissipated or had been widely distributed throughout the sample. This morphology seemed to be generally arrayed about the outer periphery of the "hemisphere;" however, some of the regions extended inward to the vicinity of the large internal void (Fig. 10b). The regions were magnetic; however, there were no unreacted particles of Al_2O_3 still present, and there was appreciable amounts of cobalt in these regions in addition to the nickel and aluminum found in the magnetic region of

Sample 13; that is, the reaction with the Al_2O_3 contamination seemed to have gone to completion. The Curie point was greater than 450°C, indicating an appreciable cobalt content.

That leaves us with the significant question of the origin of the large internal void. If the sample had uniformly cooled from the outer surface, a void would be anticipated; however, in the highly directional cooling shown, this is not anticipated. The microstructure and microchemistry adjacent to the void region is quite similar to that of the regions of Samples 13 and 23 that exhibited a coarse surface morphology and interparticle voids. This region would normally be the last to solidify; however, with the serious contamination by a low melting point material (aluminum), solidification was far from complete as these regions solidified. Perhaps then, specimen movement or reintroduction of "g" forces after partial solidification caused a lap that trapped internally what normally might have been a near-surface effect.

There is the alternate possibility that the introduction of oxygen into the melt from the Al_2O_3 caused a reaction with carbon that liberated a gas of the C_aO_b type, where a and b are integers. This could result in gas evolution at or near the reaction interface and might form a cavity of this type with access to the outer surface.

Nevertheless, the void is not due to a uniform internal shrinkage cavity and must be dismissed as an interesting but likely nonreproducible effect.

In summary, this sample demonstrated an interesting varied morphology that indicated an extremely rapid solidification in parts, and perhaps significant undercooling. The value of the specimen was compromised somewhat, however, because of significant specimen contamination by pedestal material.

CONCLUSIONS

The theoretical, analytical, and experimental techniques that we proposed for evaluating the Skylab flight samples have been tested and optimized. The results indicate that even samples of the complexity of Star-J Stellite may be reliably treated, with meaningful results generated.

The solidification characteristics of the specimens solidified in zero gravity gave rise to precipitate sizes varying from 0.5 to 0.005 of those normally encountered in as-received material. This may have been a result of more rapid cooling due to small sample size or the absence of gravity might have enhanced undercooling and caused more homogeneous nucleation.

Sample contamination from the pedestal material led to serious analytical complexities, but if this problem can be minimized in the flight samples, then the results from the specimen evaluation sequence will be meaningful. If the flight samples do prove to be contaminated, then the consequences of such contamination must be determined. This will greatly expand the analyses and the cost necessary to characterize the samples fully.

Unfamiliarity or disregard for the fundamental phase relationships occurring during solidification or superficial application of the analytical test sequence, can lead to conclusions that may be incorrect. Effort should be made to assure that these relationships are known to the contractors responsible for the sample evaluation.

REFERENCES

1. Woldman, N., Engineering Alloys, ASM Publication, 1959.

2. Herschenroeder, R. and Jenkins, E., Stellite Division of Cabot Corporation, private communication.

3. Rhines, F., Phase Diagrams in Metallurgy, McGraw-Hill Book Company, New York, 1956.

4. Hume-Rothery, W. and Raynor, G., The Structure of Metals and Alloys, Institute of Metals, 1962.

5. Kattamis, T. and Flemings, M., "Structure of Undercooled Ni-Sn Eutectic," Met. Trans., Vol. 1, 1970, p. 1449.

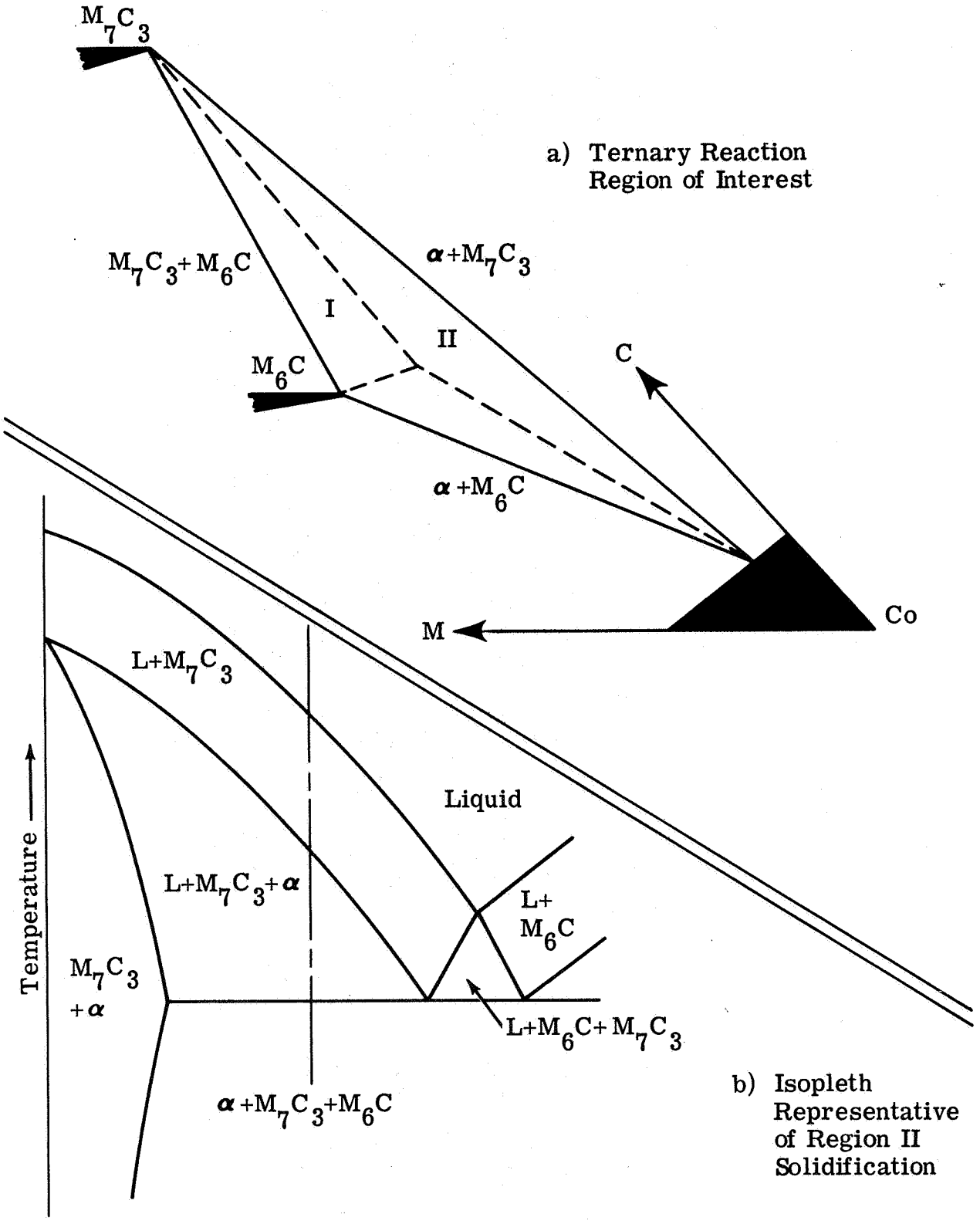

Fig. 1 Hypothetical Phase Relations for Ternary Co-M-C Alloy

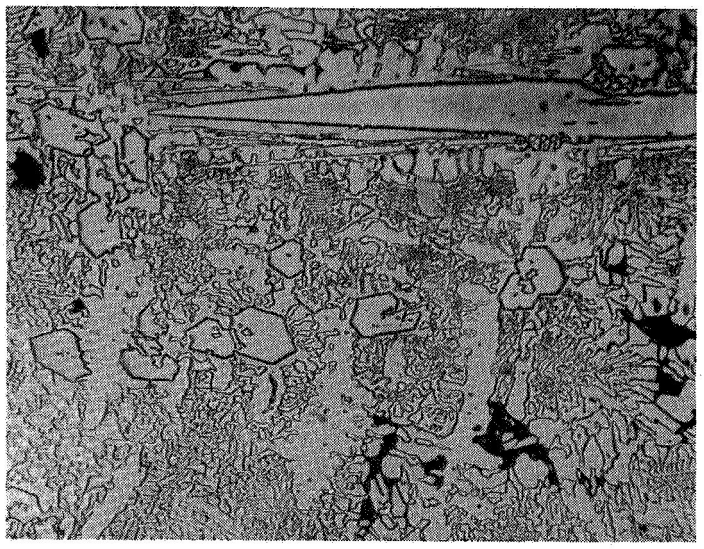

a) Optical Micrograph (150x)

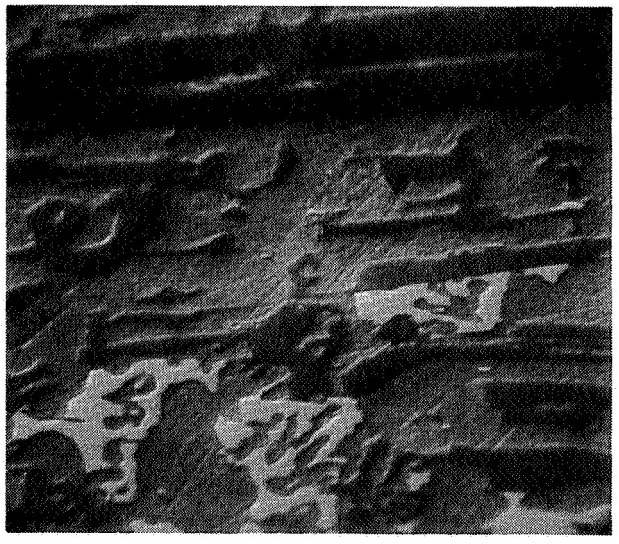

b) Scanning Electron Micrograph (800x)

Dark Grey - M_7C_3

Light Grey - α Terminal Solid Solution

White - M_6C

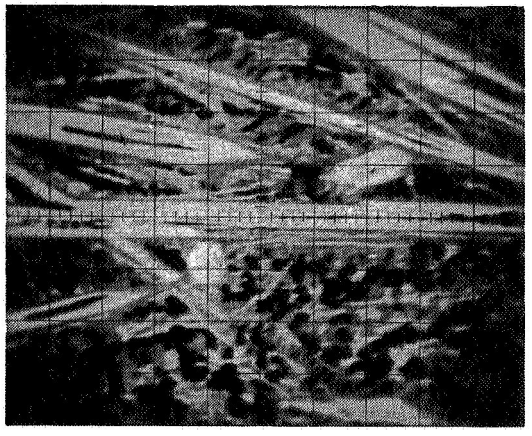

c) Electron Microprobe Image (400x)

White - M_7C_3

Grey - Terminal Solid Solution

Black - M_6C

Fig. 2 Representative Star-J Stellite Microstructures

a) (6x)

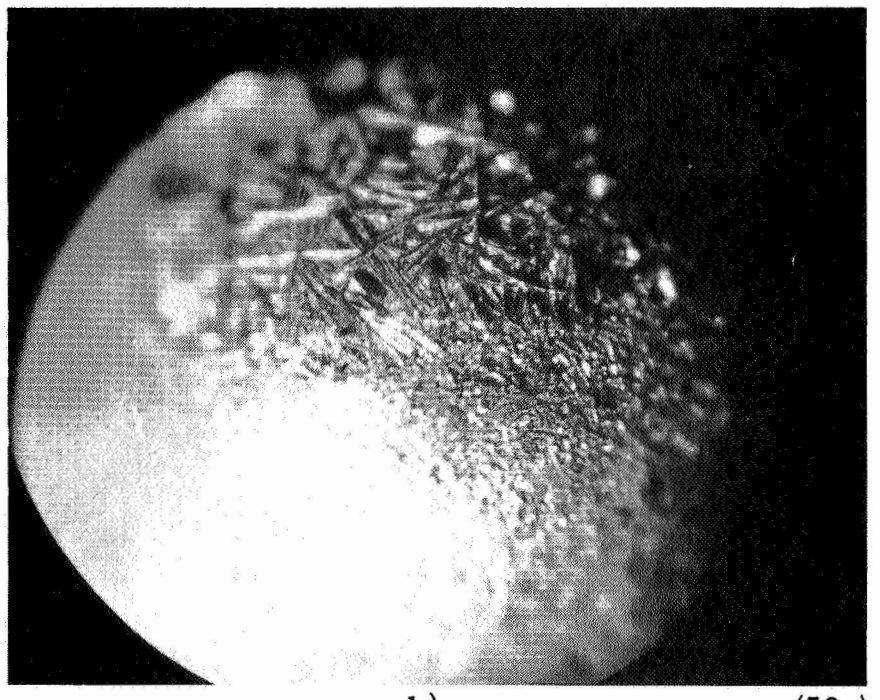

b) (50x)

Fig. 3 Surface Morphologies Representative of Sample 13, Flight 2

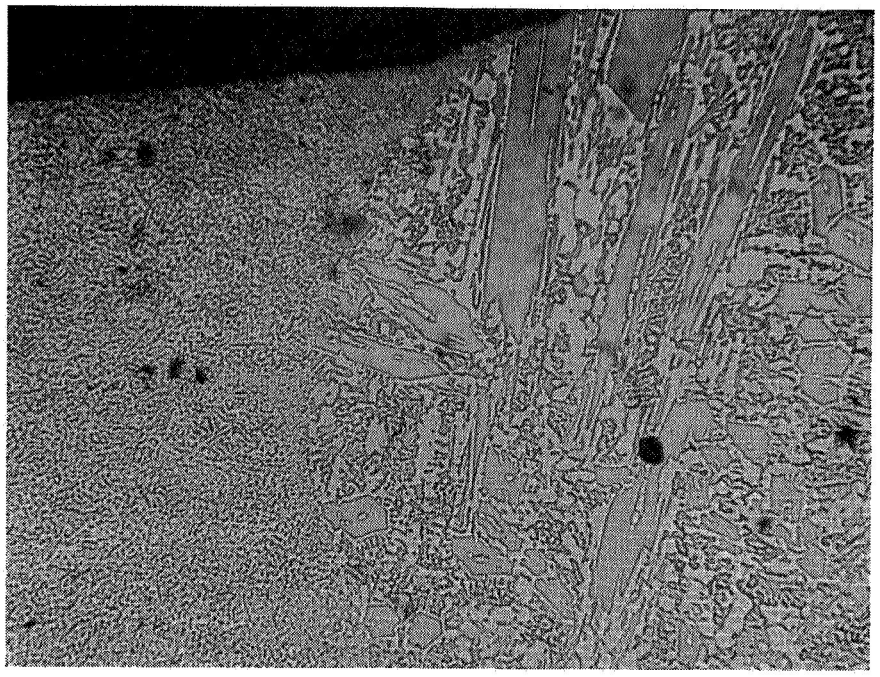

a) Transverse Section Through the Sting and Showing the Adjacent Structure of Smooth Surface Morphology (200x)

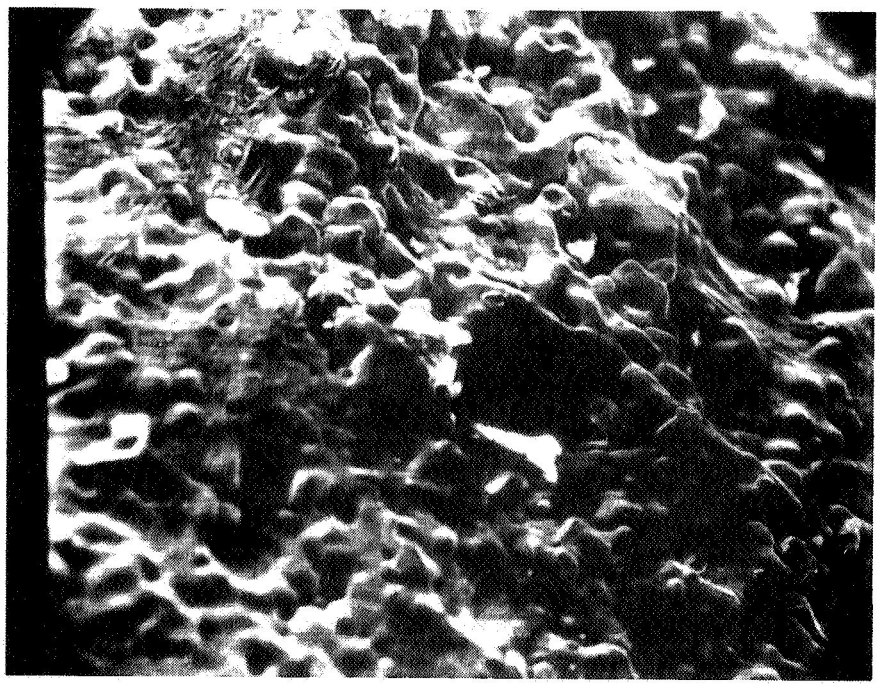

b) SEM Micrograph of Region of Smooth Surface Morphology Surface is Lacking in Primary M_7C_3 Carbides (300x)

Fig. 4 Region of Smooth Surface Morphology

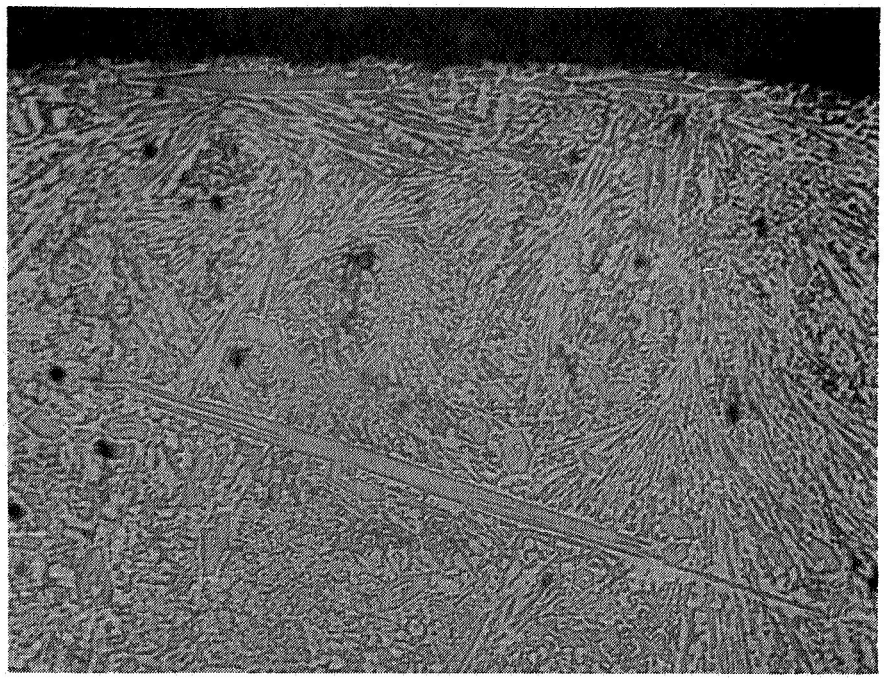

a) Optical Micrograph of Transverse Section through the Region of Intermediate Surface Roughness (150x)

b) SEM Micrograph Showing Bundles of M_7C_3 Carbides with a Nodular Interparticle Morphology. Intermediate Surface Roughness (300x)

Fig. 5 Region of Intermediate Surface Roughness

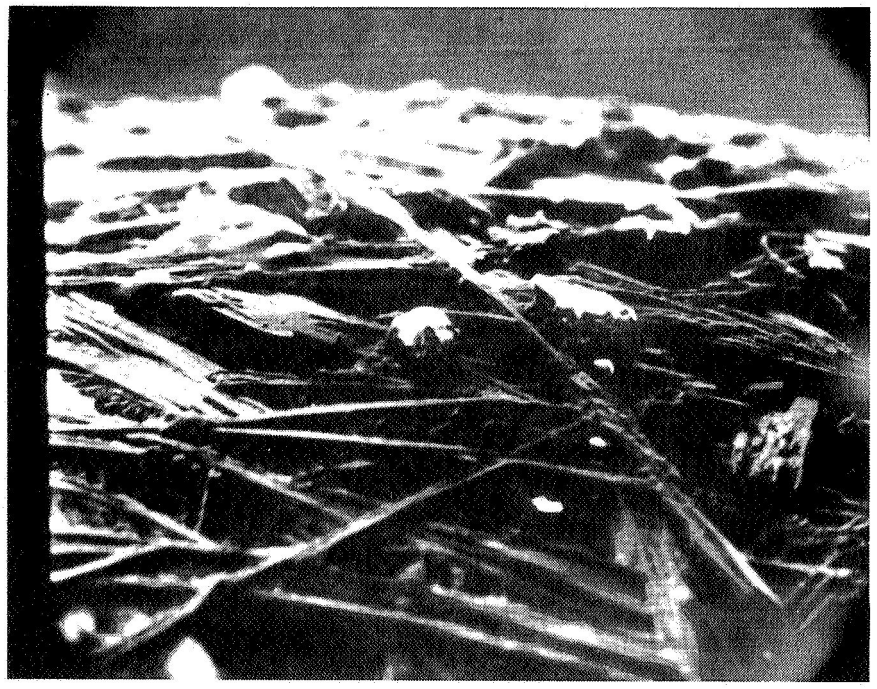

(280x)

Fig. 6 Surface Region of Coarse M_7C_3 Carbides with Large Voids Between the Needles

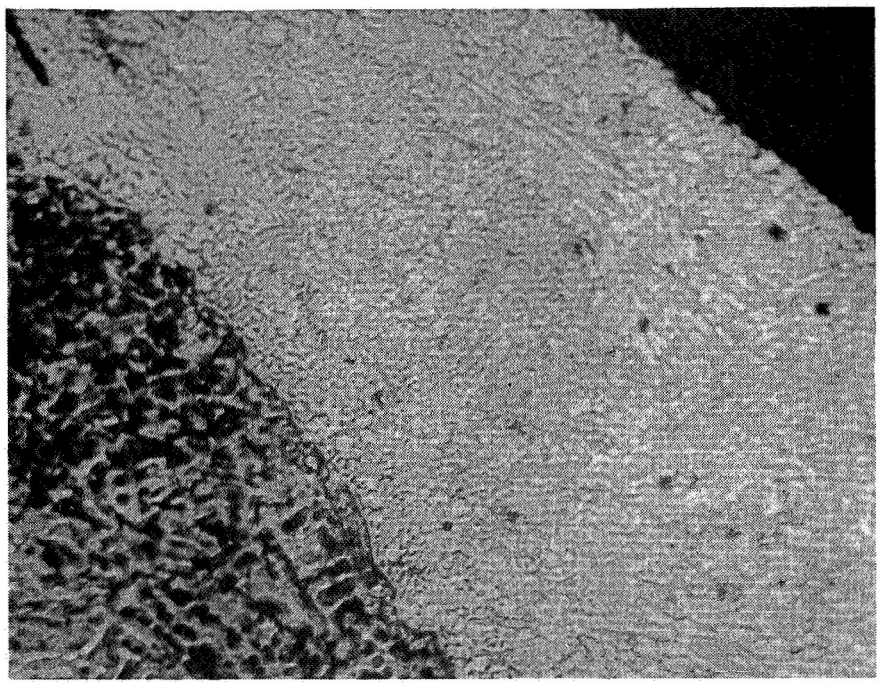

a) Micrograph Showing Well Defined Interface (200x)

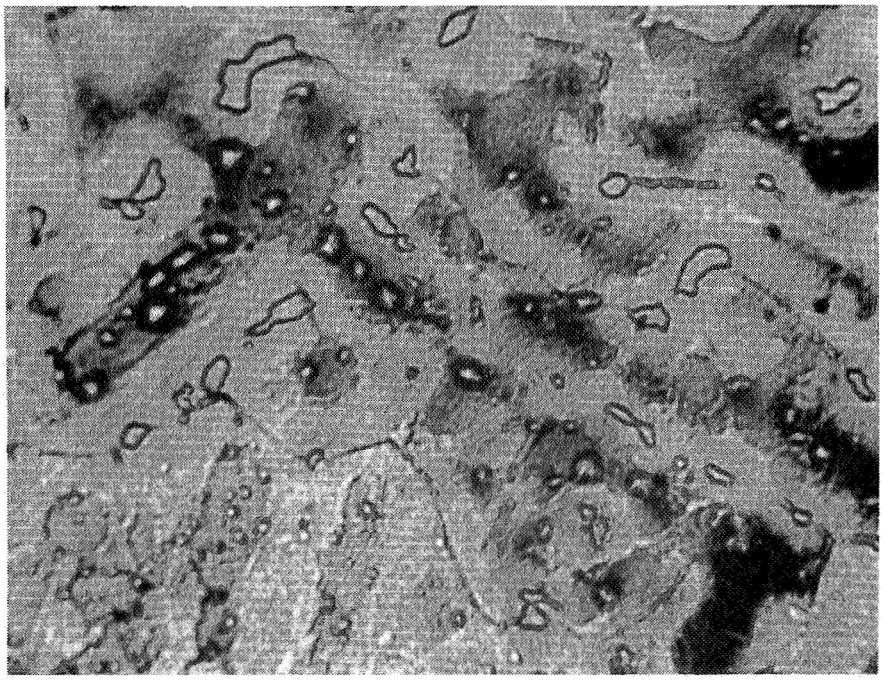

b) Microstructure of the Dendritic Interior of the Magnetic Region (775x)

Fig. 7 Microstructure of Anomalous Magnetic Region

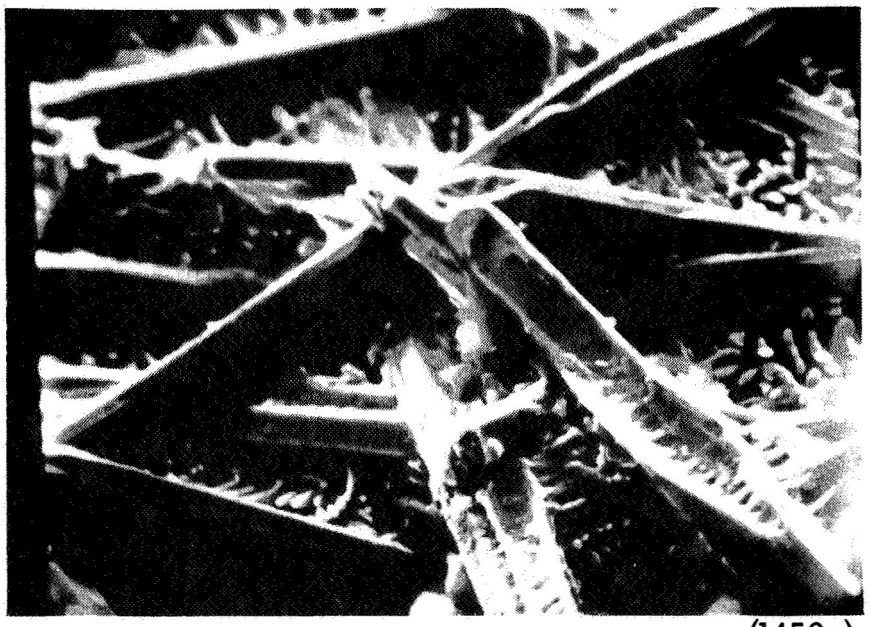

(1450x)

Fig. 8 SEM Micrograph of Coarse Surface Morphology Region Showing Interparticle Voids with some Interparticle Dendritic Secondary Structure. The hollowed or dished ends of the M_7C_3 primary carbides are also evident.

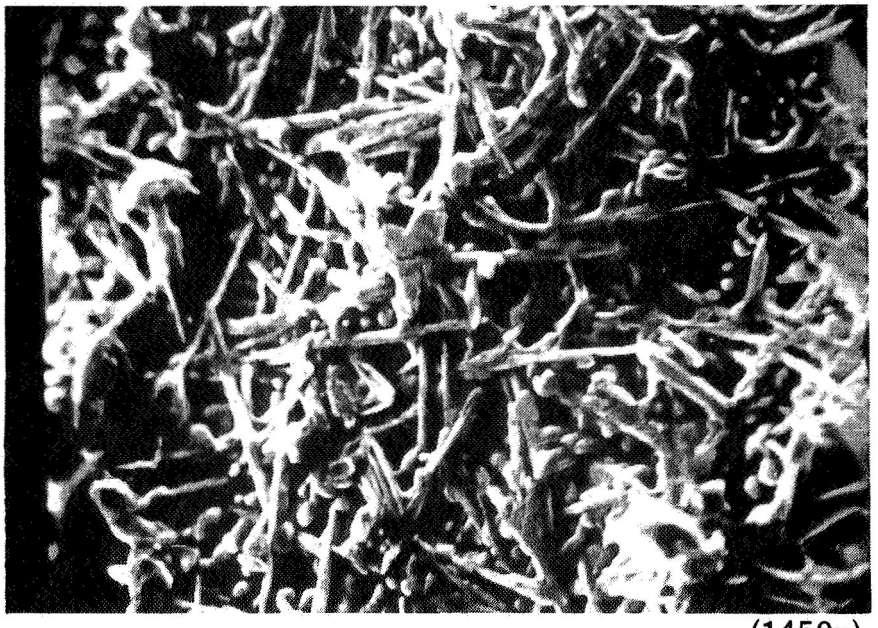

(1450x)

Fig. 9 Region of Intermediate Surface Roughness Showing Extremely Fine M_7C_3 Primary Carbides Interspersed Amomg the M_6C Nodules

a) Exterior (2x)

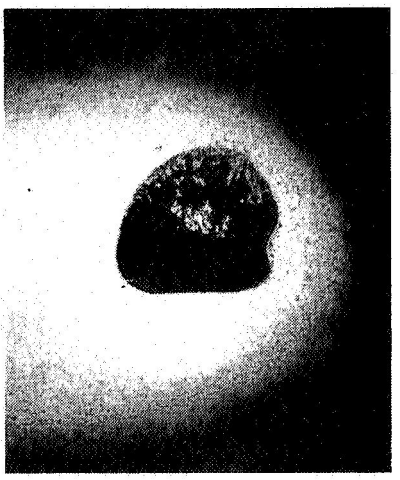

b) Interior Transverse Section Showing Lateral Void

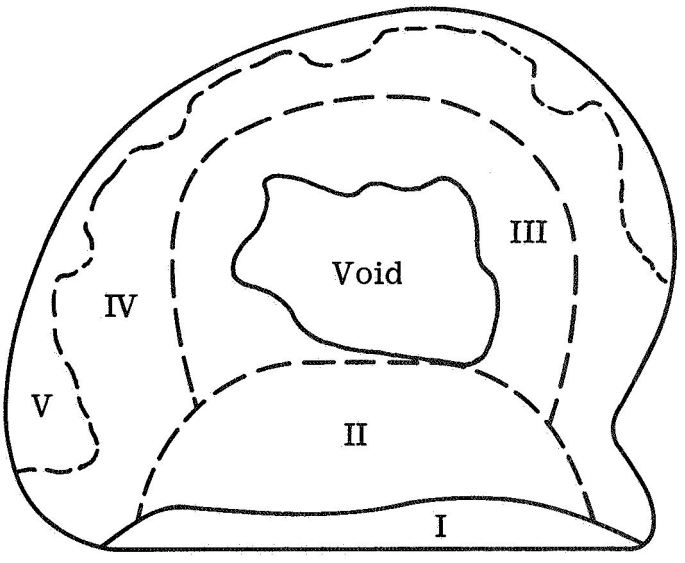

c) Schematic of the Interior Regions

Fig. 10 Macroscopic Views of Sample 1

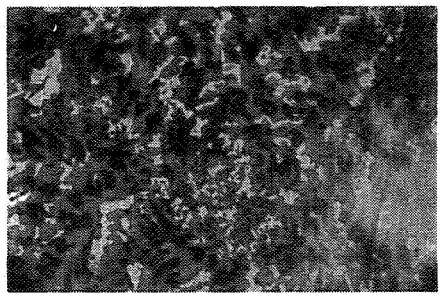

a) Region I SEM
(560x)

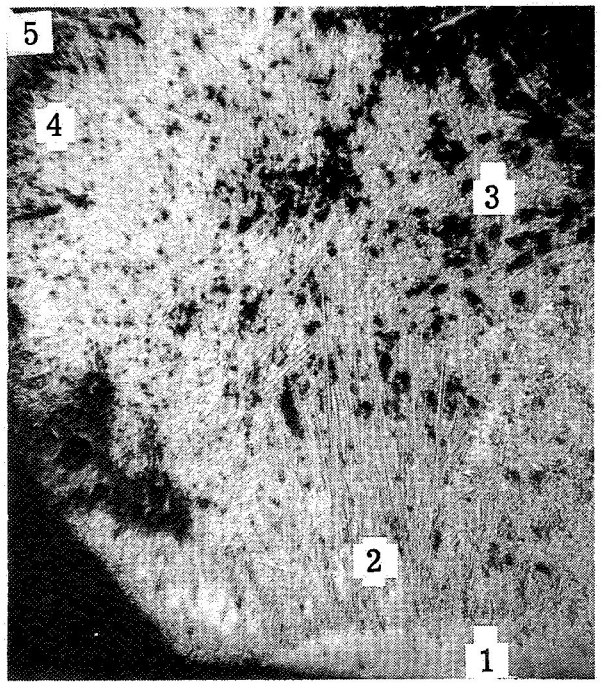

Optical (70x)

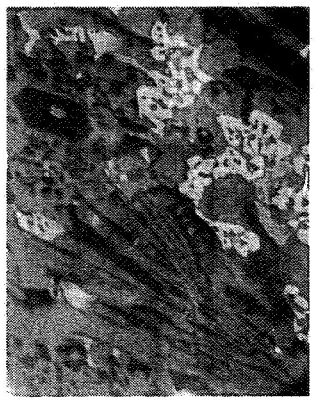

b) Region II SEM
(600x)

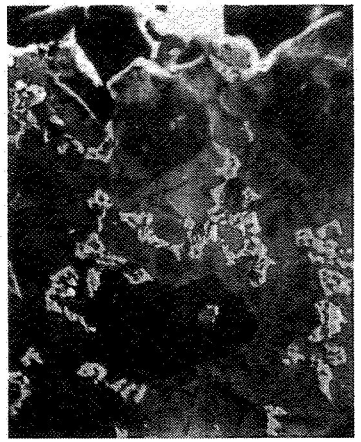

c) Region III SEM
(635x)

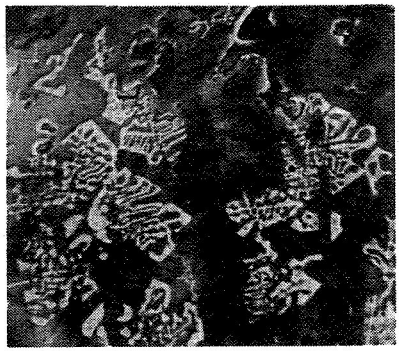

d) Region IV SEM
(675x)

e) Region V SEM
(1030x)

Fig. 11 Microstructure of the Five Distinct Regions of Sample 1

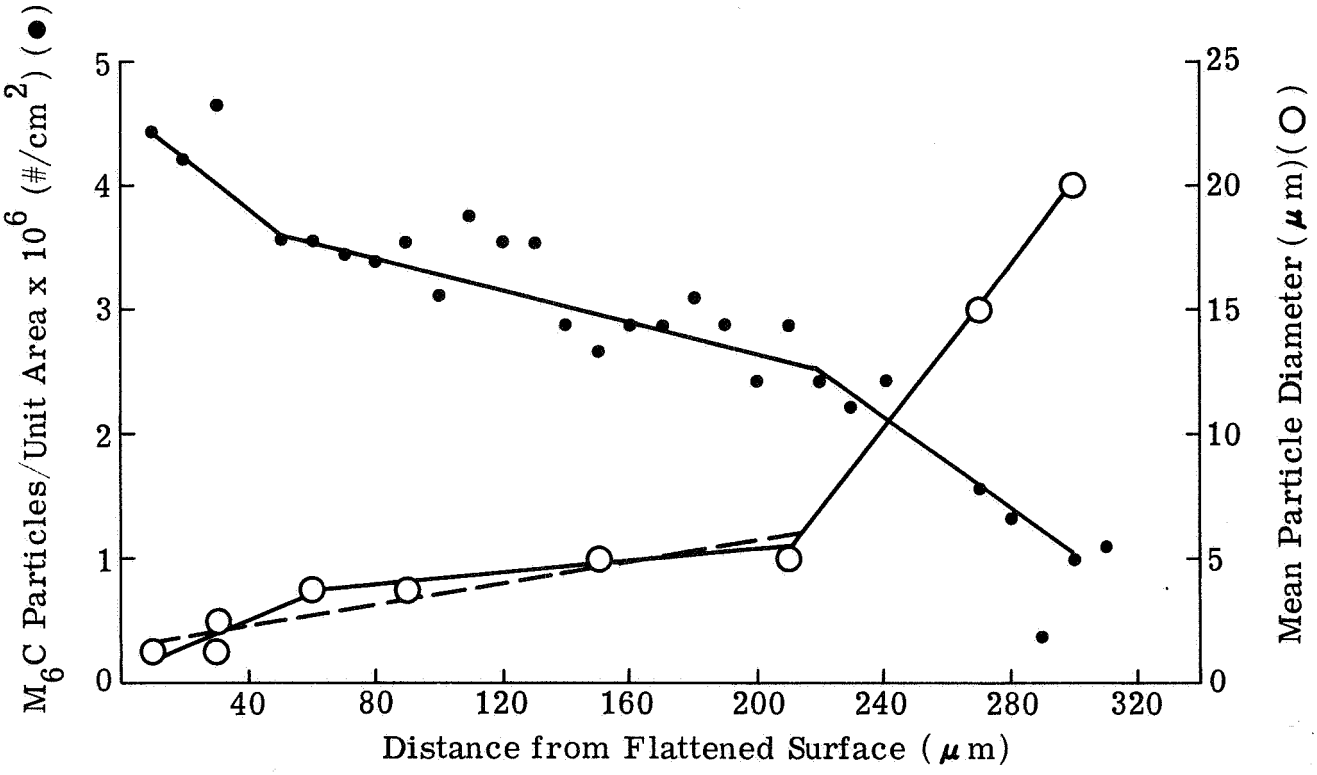

Fig. 12 Mean Particle Diameter and Particles/Unit Area of M_6C Particles in Region I of Sample 1.

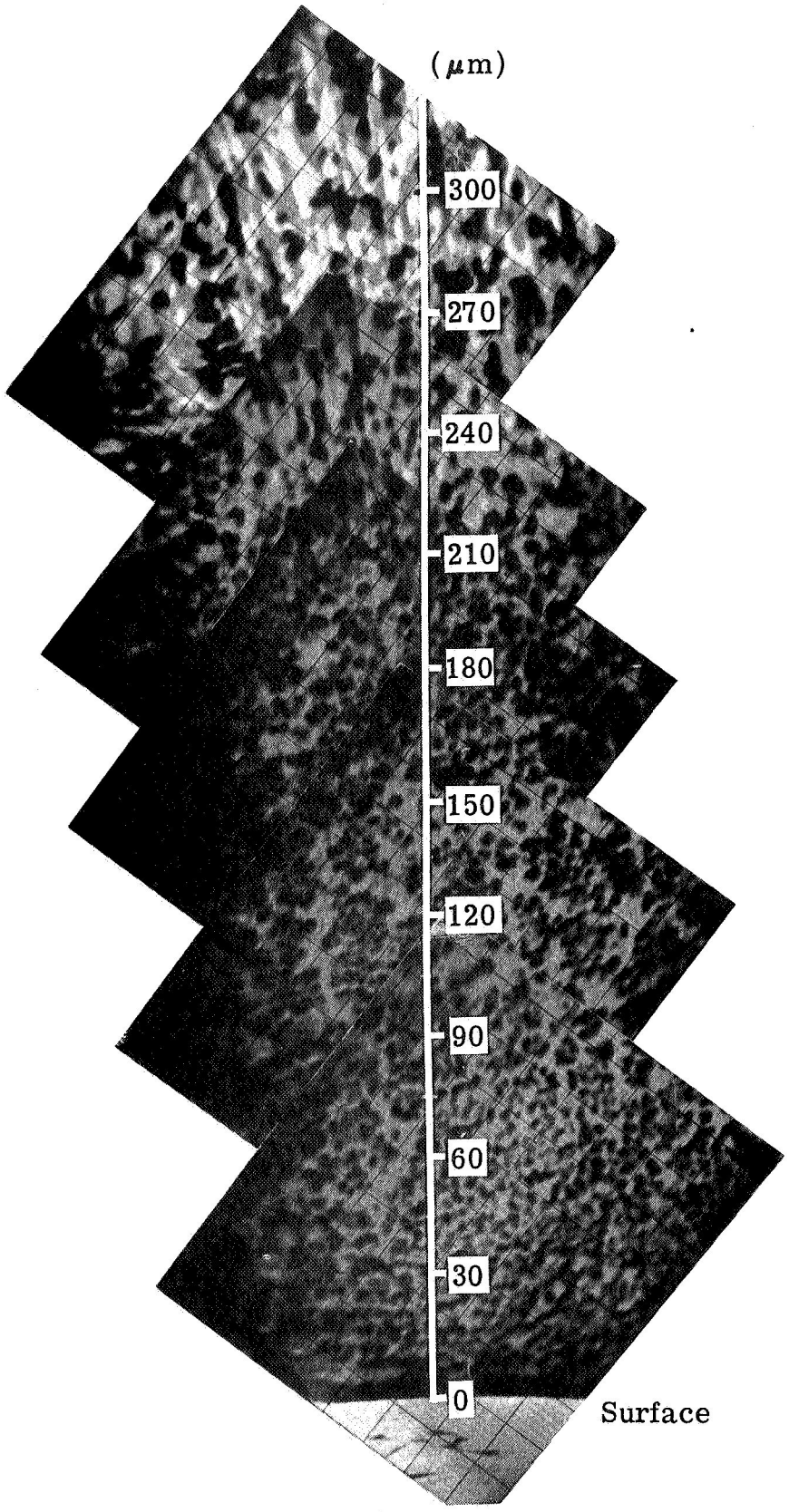

Fig. 13 Electron Microprobe Backscatter Image of Region I of Sample 1 (400x)

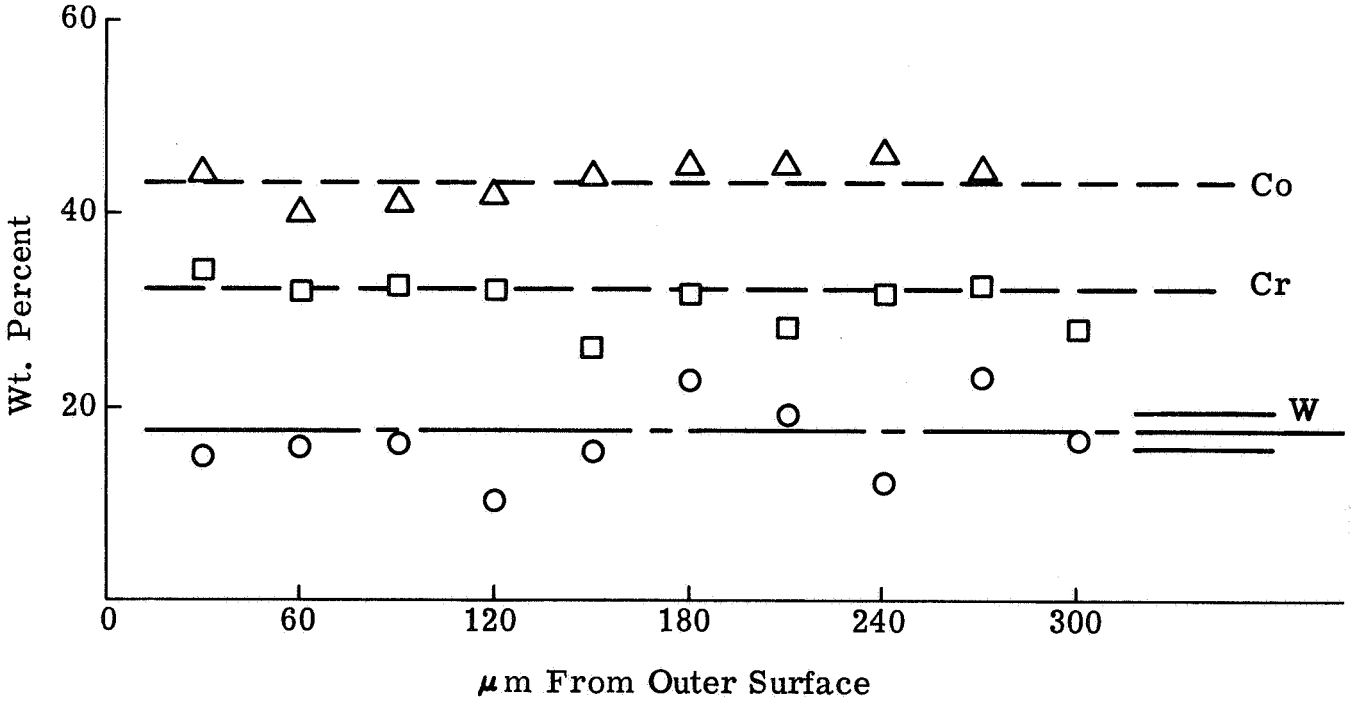

Fig. 14 Microchemistry of Sample 1 Region Shown in Fig. 13